Nano Research
2022, 15(11): 9954–9959
ISSN 1998-0124 CN 11-5974/O4
https://doi.org/10.1007/s12274-022-4543-8

Controlled growth of two-dimensional InAs single crystals via van der Waals epitaxy

Jiuxiang Dai[1], Teng Yang[2], Zhitong Jin[1], Yunlei Zhong[1], Xianyu Hu[1], Jingyi Zou[3], Weigao Xu[4], Tao Li[1], Yuxuan Lin[5], Xu Zhang[3], and Lin Zhou[1] (✉)

[1] *School of Chemistry and Chemical Engineering, Frontiers Science Centre for Transformative Molecules, Shanghai Jiao Tong University, Shanghai 200240, China*
[2] *Shenyang National Laboratory for Materials Science, Institute of Metal Research, Chinese Academy of Sciences, Shenyang 110016, China*
[3] *Department of Electrical and Computer Engineering, Carnegie Mellon University, Pittsburgh, PA 15213, USA*
[4] *Key Laboratory of Mesoscopic Chemistry, School of Chemistry and Chemical Engineering, Nanjing University, Nanjing 210023, China*
[5] *Department of Electrical Engineering and Computer Sciences, University of California, Berkeley, CA 94720, USA*

© Tsinghua University Press 2022

Received: 19 February 2022 / **Revised:** 2 May 2022 / **Accepted:** 16 May 2022

ABSTRACT

Two-dimensional (2D) indium arsenide (InAs) is promising for future electronic and optoelectronic applications such as high-performance nanoscale transistors, flexible and wearable devices, and high-sensitivity broadband photodetectors, and is advantageous for its heterogeneous integration with Si-based electronics. However, the synthesis of 2D InAs single crystals is challenging because of the nonlayered structure. Here we report the van der Waals epitaxy of 2D InAs single crystals, with their thickness down to 4.8 nm, and their lateral sizes up to ~ 37 μm. The as-grown InAs flakes have high crystalline quality and are homogenous. The thickness can be tuned by growth time and temperature. Moreover, we explore the thickness-dependent optical properties of InAs flakes. Transports measurement reveals that 2D InAs possesses high conductivity and high carrier mobility. Our work introduces InAs to 2D materials family and paves the way for applying 2D InAs in high-performance electronics and optoelectronics.

KEYWORDS

two-dimensional materials, van der Waals epitaxy, indium arsenide, nonlayered material

1 Introduction

The III-V semiconductors are ideal for numerous electronic and optoelectronic applications such as high-performance transistors [1, 2], photodetectors [3, 4], light emitters [5], and photovoltaics [6, 7] due to their high carrier mobilities, and narrow and direct band gaps. Two-dimensional (2D) III-V compounds are highly demanded in the integration of III-V semiconductors with Si technology, miniaturization devices, flexible and wearable devices, and heterostructures because of their superb physical properties, flexibility, high compatibility with current semiconductor manufacture techniques, and the ease of integration with Si-based devices [8–12]. However, the nonlayered structure with strong covalent bonds in three dimensions makes it challenging to obtain 2D III-V semiconductors.

Indium arsenide (InAs) is an important member of III-V compounds. It has a narrow direct bandgap (~ 0.390 eV for wurtzite structure and ~ 0.350 eV for zinc blende structure), high electron mobility, and high photoresponse [4, 13–15]. Thus, InAs is widely used for high-speed and low power consumption devices, and highly sensitive photodetectors with a broadband spectral response from ultraviolet to infrared [8, 16–18]. Ali Javey et al. creatively integrated ultrathin InAs film on SiO_2 for high-performance nanoscale transistors, demonstrating the merits of ultrathin InAs film [19]. Even though 2D InAs is easy to heterogeneously integrate and nanofabricate, its large surface area is beneficial to photodetectors and sensors, and research of low-dimensional InAs has been mainly focused on quantum dots and nanowires [18, 20–22]. High-quality 2D (sub-10 nanometers) InAs has not been reported, let alone the scalable synthesis of 2D InAs single crystals.

Here, we synthesize 2D InAs flakes via van der Waals (vdW) epitaxy. The lateral size of single-crystal InAs flakes is up to ~ 37 μm, and the thickness of flakes is down to 4.8 nm. We use atomically flat mica as the substrate. In contrast to covalent bonds in conventional epitaxy, the weak vdW interaction between mica substrate and InAs facilities 2D InAs growth without lattice constraint and its easy integration with Si technologies through transfer. The as-grown InAs single crystals are homogenous and of high crystalline quality. The thickness-dependent optical properties and electrical characteristics of 2D InAs are investigated. The carrier mobility is ~ 25 $cm^2 \cdot V^{-1} \cdot s^{-1}$ at room temperature. Our work provides a scalable method to grow 2D InAs without lattice restriction, inventing a new member to 2D materials family, and paving the way for miniaturization InAs based devices and integrations.

Address correspondence to linzhou@sjtu.edu.cn

2 Results and discussion

Bulk wurtzite InAs belongs to the $P6_3mc$ space group with lattice parameters $a = b = 4.284$ Å and $c = 6.996$ Å [23]. The bulk InAs unit cell includes two In atoms and two As atoms. Each In anion is in hexagonal coordination with four As neighbors, and the anions of As coordinate with the four cations of In to form a tetrahedron with four As–In bonds. The hexagonal arrangement of atoms is exhibited in the top view ((0001) plane, lower right in Fig. 1(a)). As shown in Fig. 1(a), the structure of bulk InAs clearly illustrates its nonlayered feature. 2D InAs flakes are synthesized in a home-built tube furnace. Figure 1(b) depicts a schematic image of the growth setup. We use pure InAs powder as the precursor and keep its temperature at 770–850 °C. Substrates are placed 9.5 cm downstream from the InAs source. The carrier gas is 50 standard cubic centimeters per minute (sccm) Ar gas (see details in the Experimental section). Among the commonly used substrates including SiO_2, sapphire, and fluorophlogopite mica, 2D InAs can only grow on mica substrates, but is prone to forming particles on SiO_2 and sapphire under the same growth condition (Fig. S1 in the Electronic Supplementary Material (ESM)). A possible mechanism is that mica's surface is atomically flat and free of dangling bonds, facilitating the migration of InAs molecules on the mica surface [24, 25]. Moreover, the triple symmetric structure of mica (001) matches the symmetry of wurtzite InAs (0001). The lattice of InAs is commensurate with mica via 5 × 5 (InAs)/4 × 4 (mica) supercell matching, enabling the epitaxy growth of InAs on mica (Fig. 1(c) and Fig. S2 in the ESM).

Optical and atomic force microscopy (AFM) images show that InAs flakes of various thicknesses have triangular or truncated triangular shapes (Figs. 1(d) and 1(e), and Fig. S3 in the ESM). The thinnest InAs flake we obtained is ~ 4.8 nm thick (Fig. 1(e)), and the grain size of a single InAs flake is up to ~ 37 μm (Fig. S3(a) in the ESM). Figure 1(f) and Fig. S4 in the ESM reveal the thinnest sublayer InAs (~ 0.35 nm) grown on InAs single crystal with the same orientation. Since the subunit cell thickness of InAs is ~ 0.35 nm along the [0001] direction (Fig. 1(c)), the measured sublayer thickness suggests a layer-by-layer growth mode in the formation of the nonlayered 2D InAs crystals.

Considering that the bulk InAs crystal is polymorphism, we carefully characterize the structure and elemental distribution of as-grown 2D InAs flakes. X-ray diffraction (XRD) spectrum reveals the diffraction peak at 25.6°, corresponding to the InAs (0002) lattice plane (Fig. S5 in the ESM). It indicates [0001] is the preferred growth crystal plane on mica. Low-resolution transmission electron microscopy (TEM) image of a typical InAs flake reveals a perfect triangular shape, consistent with the structure along the [0001] direction (Fig. 2(a)). Moreover, the corresponding atomic-resolved TEM shows perfect periodicity of the atom sites without distinct defects, indicating the high quality of the as-grown InAs (Fig. 2(b)). Each In atom is surrounded by four As atoms, matching well with the top-view atomic model of InAs (the inset of Fig. 2(b)). The lattice spacing of 0.21 nm is consistent with the $(11\bar{2}0)$ planes of wurtzite InAs [23]. Additionally, the selected area electron diffraction (SAED) presents a single set of hexagonal diffraction spots, unveiling the hexagonal symmetry of the crystals (Fig. 2(c)). The $(10\bar{1}0)$ lattice plane spacing in Fig. 2(c) is measured to be 0.37 nm, in agreement with wurtzite InAs [23]. Furthermore, the SAED patterns of several locations on a single flake show identical hexagonal patterns and locations, confirming the single-crystal nature of the InAs flake (Fig. S6 in the ESM). Quantitative elemental analysis of the energy-dispersive X-ray spectroscopy (EDS) indicates that the main elements in the flake are In and As (Fig. 2(f)). Moreover, EDS elemental maps display uniformly distributed In and As elements in the InAs flake (Figs. 2(d) and 2(e)). The atomic ratio of In to As is about 53:47, which is close to the stoichiometric ratio of InAs.

To access the chemical composition and bonding type of the as-grown InAs, we perform X-ray photoelectron spectroscopy (XPS) measurement. The high-resolution In 3d spectra show two pairs of peaks at 444.06 and 451.57 eV, as well as 445.09 and 452.66 eV, corresponding to the InAs and In_2O_3, respectively (Fig. 3(a)) [26]. Figure 3(b) exhibits the As $3d_{5/2}$ and $3d_{3/2}$ peaks, located at 40.34 and 41.11 eV, are attributed to the In–As bonds [26]. Both In 3d and As 3d spectra reveal oxides in the sample. The oxides might be the natural oxide layer formed upon InAs after exposure to air, similar to the case of InAs nanowires [26]. The atomic ratio of In:As is around 47:53. Therefore, both XPS and EDS indicate the as-grown InAs is stoichiometric.

In order to precisely control the thickness and realize 2D InAs growth, we finely tune the temperature and growth time. Furthermore, we investigate their influences on the thickness of InAs flakes. We vary the growth temperature at 770, 790, 810, 830,

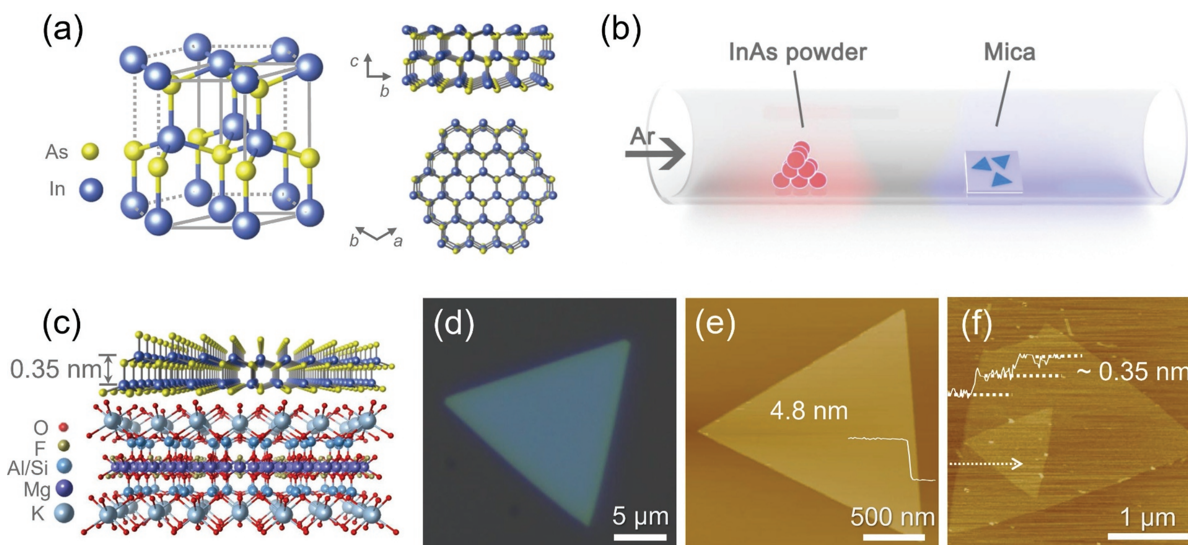

Figure 1 Growth and morphology characterizations of 2D InAs flakes. (a) Atomic structure of InAs. The golden spheres are As atoms, and the blue spheres are In atoms. (b) Schematic illustration of the growth setup for the synthesis of 2D InAs. (c) Structure of 2D InAs flakes on mica. (d) Representative optical image of 2D InAs flake. (e) AFM image of a 2D InAs flake with the thickness of 4.8 nm. (f) AFM morphology image of InAs sub-unit cells with the thickness of about 0.35 nm.

Nano Res. 2022, 15(11): 9954–9959

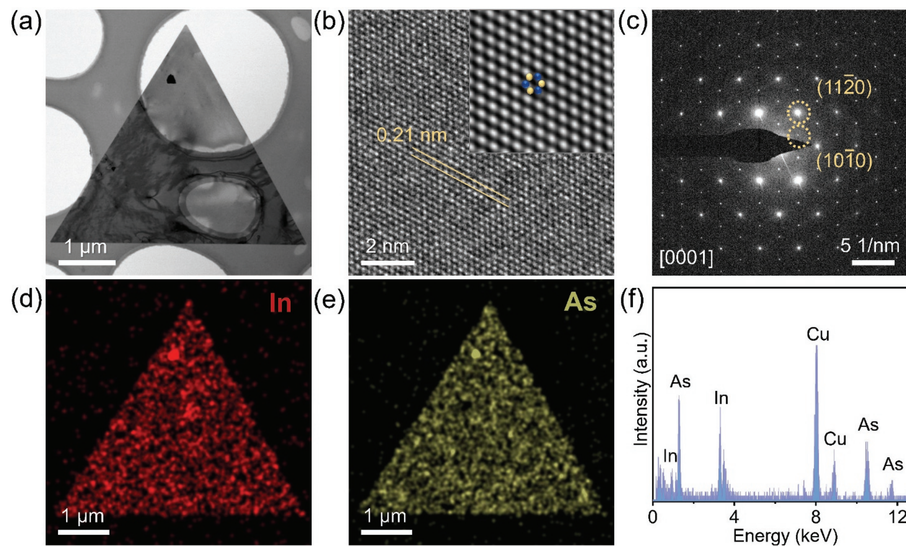

Figure 2 TEM characterization of the 2D InAs flake. (a) Bright-field TEM image of a typical 2D InAs flake. (b) High-resolution TEM image of the 2D InAs flake. Inset is the top-view atomic model of InAs. The golden spheres are As atoms, and the blue spheres are In atoms. (c) Corresponding SAED pattern of the 2D InAs flake. Elemental maps of (d) In and (e) As of the 2D InAs flake shown in (a). (f) The EDS spectrum of the 2D InAs flake.

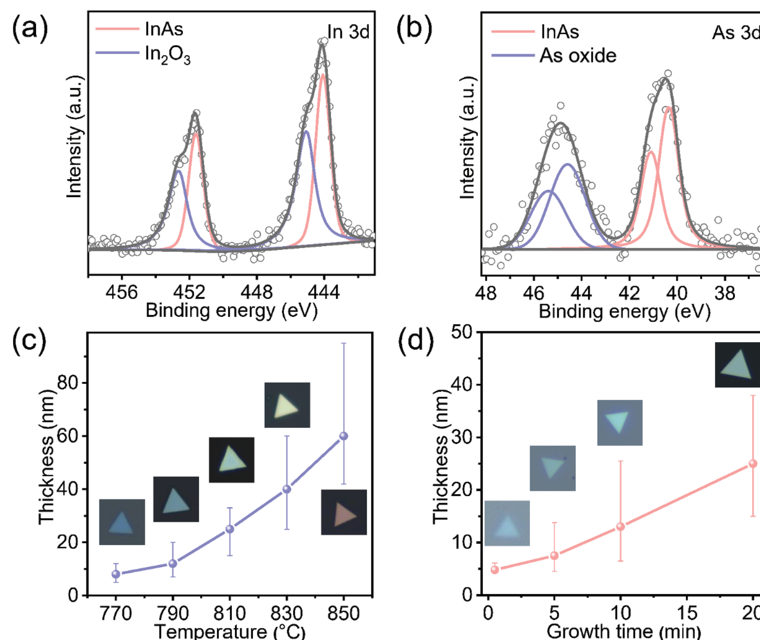

Figure 3 XPS spectra of (a) In 3d and (b) As 3d peaks. (c) Statistical thickness of 2D InAs flakes grown at varying growth temperatures from 770 to 850 °C. Insets are the corresponding typical optical images. (d) Statistical thickness of 2D InAs flakes grown at varying growth time from 0.5 to 20 min. Insets are the related optical images.

and 850 °C and keep other conditions the same. As shown in Fig. 3(c), the color of typical InAs flakes grown at different growth temperatures changes from light cyan to pink. Furthermore, the median thickness changes from 8 to 60 nm, and the thickness variance increases when raising the growth temperature. Thus, higher temperature often leads to thicker flakes and larger variations of thicknesses. The growth temperature determines the partial pressure of reactants and influences growth processes. Briefly, as the temperature of the InAs source increases, the vapor pressure of reactants dramatically rises, resulting in thicker flakes. Moreover, the growth is thermodynamically controlled at high temperature, thus prone to form structures that have the lowest total energy of the system (symmetries). Therefore, the as-grown flakes should be thicker because of the three-dimensional (3D) InAs crystal structure. In contrast, the growth is mainly kinetically controlled at low temperature. Adatoms on the surface quickly attach to the fastest growth front at edge regions, leading to thinner flakes [27, 28]. The growth time also has a significant impact on the thickness of flakes. As the growth time increases from 0.5 to 20 min, the median thickness changes from 5 to 25 nm (Fig. 3(d)). It is easy to interpret that a longer growth time allows more precursors to participate in the vertical growth of flakes [29, 30]. Both median thickness and thickness range become large with increasing growth time. In short, a relatively low temperature and short growth time are prone to synthesizing 2D InAs flakes.

We investigate the optical properties of InAs flakes through second-harmonic generation (SHG) and Raman spectroscopy. A considerable SHG intensity is detected from an InAs flake, revealing the nonlinear optical properties of 2D InAs flake (Fig. 4(a)). Two prominent Raman peaks at ~ 213–217 and ~ 237 cm^{-1}, assigned as the transverse optical (TO) and the longitudinal optical (LO) modes, respectively, appear in InAs flakes with diverse thicknesses (Fig. 4(b)). From group theory analysis, the TO and

LO modes are both the 2-fold degenerate E modes of the C_{3v} point group. Both LO and TO modes have In and As atoms displacing in the opposite in-plane directions, and are visualized in the inset of Fig. 4(b). Interestingly, the TO mode shows a strong red shift when decreasing InAs's thickness from 63 to 5.5 nm, which can be understood by the thickness-dependent dielectric constant (screening effect). From our density functional theory (DFT) calculation, dielectric constant (or the screening effect) increases with the decreasing thickness, leading to a weakened restoration force of the TO mode and thus a red shift of the Raman shift (Table S1 and more discussions in the ESM). Besides LO and TO phonon peaks, there is another phonon peak centered around 228.0 cm^{-1}, which can be attributed to the surface optical (SO) phonons (Fig. S8 in the ESM). Such SO phonon modes are common in semiconductor nanomaterials [31–33]. Normally, they are correlated to the shape of the semiconductor under examination and to the dielectric properties of both the semiconductor and the external medium [31]. Raman maps of a typical InAs flake show uniform intensity over the whole flake, indicating the high spatial homogeneity of the as-grown InAs (Figs. 4(d)–4(f)).

We further characterize the electronic properties of 2D InAs flakes through transport measurements. We first pre-patterned Cr/Au electrodes on a 300 nm SiO_2/Si substrate using photolithography followed by metal deposition. Then we transfer the InAs flake onto the channel region through the polystyrene (PS) assistant transfer method (Fig. 5(a)) [34]. The linear I_{DS}–V_{DS} curve reveals that ohmic contacts are formed between the InAs channel and the Cr/Au metal electrodes (Fig. 5(b)). The large densities of donor-type surface states pin the Fermi level above the conduction band minimum of InAs, thus forming ohmic contact between InAs and metals (Fig. S9 in the ESM) [35]. The resistance without gate is ~ 450 Ω. The magnitude of drain current at V_{DS} = 0.5 V approaches 1 mA in the saturation regime, and the InAs device exhibits high conductivity. The InAs device shows a weak gate-dependence, corresponding to a heavily doped n-type semiconductor (Fig. 5(c)). We estimate the field-effect mobility μ by

$$\mu = \frac{L}{W\left(\frac{\varepsilon_0 \varepsilon_r}{d}\right) V_{DS}} \frac{dI_{DS}}{dV_{GS}} \quad (1)$$

where L, W, and d are the channel length, width, and the thickness of the SiO_2 layer, respectively. The ε_0 and ε_r are the vacuum dielectric constant and the dielectric constant of SiO_2, respectively. I_{DS} and V_{GS} are the current between the source and drain and the voltage between the gate and source, respectively. The values of L, W, ε_r, ε_0, V_{DS}, and d are 2.5 μm, 10 μm, 3.9, 8.85 × 10^{-12} $F \cdot m^{-1}$, 0.5 V, and 300 nm, respectively. The carrier mobility is around 25 $cm^2 \cdot V^{-1} \cdot s^{-1}$ at 300 K. Moreover, considering the two-terminal device configuration and contact influence, it is anticipated that the as-grown 2D InAs has better intrinsic transport properties. The low resistance and decreased mobility should be attributed to large densities of surface states on InAs flake which pin the surface Fermi level above the conduction band and degrade the electron mobility in the flake [26]. We envisage that modifications of surface states can further boost the transport performance of 2D InAs flakes.

3 Conclusions

In summary, we have synthesized 2D InAs flakes through vdW epitaxy. The as-grown 2D InAs has a triangular or truncated triangular shape with lateral size up to tens of micrometers. Low temperature and short growth time are prone to growing thin InAs flakes. The InAs flakes show high crystalline quality, thickness-dependent optical properties, and mobilities comparable with traditional 2D transition metal dichalcogenides. Our work introduces a new member for 2D family and paves this promising material the way for high-performance nanoelectronic and optoelectronic applications.

4 Experimental section

4.1 Sample preparation

InAs flakes were grown in a quartz tube with a horizontal single-temperature-zone tubular furnace under atmospheric pressure. 20 mg InAs powder (99.99%, Macklin) was in a quartz boat and placed at the center of the heating zone. Fluorophlogopite mica ($KMg_3(AlSi_3O_{10})F_2$) substrates (1 cm × 1 cm) were positioned in another quartz boat and placed 9.5 cm downstream from InAs precursor. The tube was evacuated and flushed with Ar gas to provide an oxygen-free environment. Then the temperature was ramped to 770–850 °C in 20 min and maintained at the temperature for 0.5–20 min under 50 sccm Ar flow. After the growth, the furnace was rapidly cooled down to room

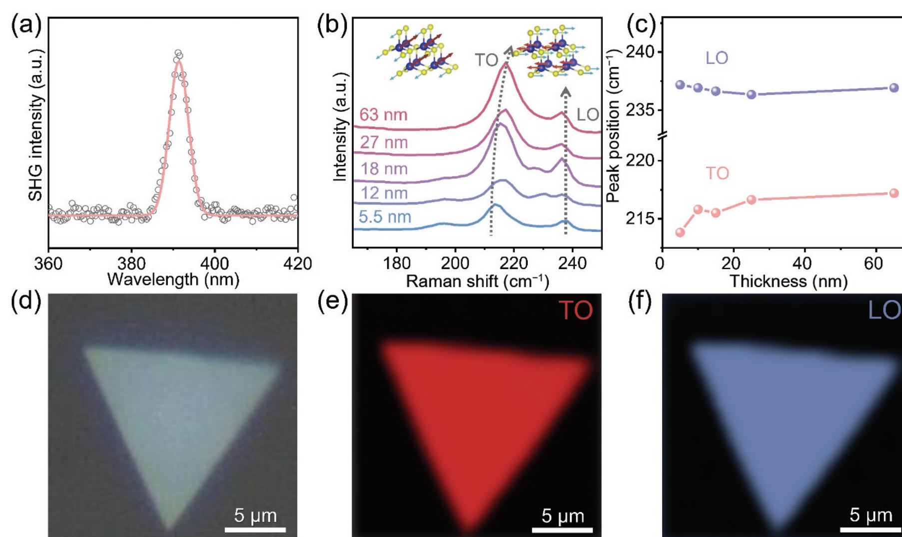

Figure 4 (a) SHG signals of the as-grown 2D InAs flake. (b) Thickness-dependent Raman spectra of as-grown 2D InAs flakes on mica. Insets are the corresponding atomic displacements of TO and LO modes. (c) Thickness-dependent Raman peak positions of TO and LO modes. (d) Optical images and the corresponding Raman intensity mappings of (e) TO and (f) LO modes of a typical triangular InAs flake grown on mica.

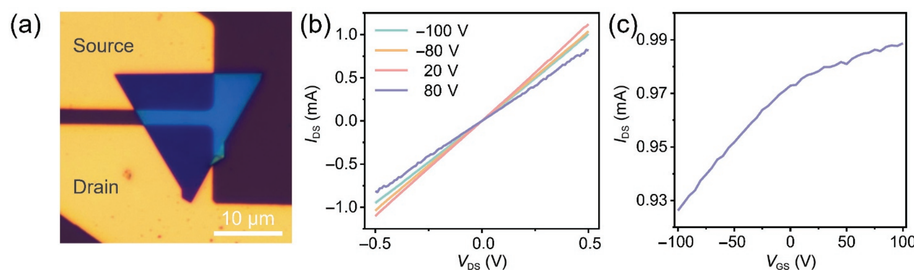

Figure 5 Electrical properties of 2D InAs flake. (a) Typical optical image of an InAs field-effect transistor (FET). (b) Output characteristics of the device at different gate voltages. (c) Transfer characteristic of the InAs FET at a fixed source-drain voltage of V_{DS} = 0.5 V.

temperature with the assistance of electric fans.

4.2 Sample transfer

The as-grown 2D InAs flakes on mica could be transferred onto an arbitrary substrate or TEM grid using a wet transfer approach. Briefly, the mica substrate was spin-coated with the PS at 3,000 rpm for 60 s and baked at 80 °C for 30 min. The PS solution was prepared with 13 g PS particles (280,000 g·mol^{-1}) and 100 mL toluene. The PS film was scraped off the edges of the mica. Then the sample was dipped into water. After that, PS/InAs was separated from mica and transferred onto a target substrate. Finally, the transferred sample was dried at 110 °C for 20 min, followed by toluene immersion for 12 h to dissolve the PS.

4.3 Sample characterization

The morphology, microstructure, and chemical constituents of the 2D InAs flakes were analyzed and characterized via optical microscopy (OM, Leica DM4000M), AFM (Bruker Multimode 8), confocal Raman spectroscopy (Renishaw inVia Qontor) with a 532 nm laser, XPS (Thermo Scientific NEXSA), and XRD (Bruker D8 ADVANCE Da Vinci). SHG was performed on Raman spectroscope (Horiba HR Evolution) with a femtosecond laser as the excitation source. Polymethyl methacrylate (PMMA) was spin-coated on InAs samples before Raman and SHG measurement to prevent oxidation. TEM images, SAED patterns, and EDS elemental mapping were taken from a TEM operating at 200 kV (Thermo Scientific TALOS F200X). The electrical properties were measured using a semiconductor parameter analyzer (Keithley 4200-SCS) in ambient air.

4.4 Density functional calculation

First-principles calculations based on DFT were performed using the local density approximation (LDA) presented by Cepeley–Alder (CA) functional, as implemented in the Vienna *ab initio* simulation package (VASP) [36, 37]. The projected augmented wave (PAW) method with a plane-wave basis set was used with a cutoff energy of 520 eV [38]. Monkhorst–Pack *k* meshes of 8 × 8 × 4 and 8 × 8 × 1 were adopted to represent the reciprocal first Brillouine zone of bulk and two-dimensional InAs structures, respectively [39]. The convergence criteria for the energy and force were set to 10^{-5} eV and 0.01 eV·Å^{-1}, respectively. The dielectric and vibrational properties were calculated based on the finite displacement method. The phonon modes were visualized by the XCrysDen software [40].

Acknowledgements

This work was supported by the National Key Basic Research Program of China (No. 2021YFA1401400), the start-up funds of Shanghai Jiao Tong University, the National Natural Science Foundation of China (Nos. 52103344, 52031014, 22022507, and 51973111), the National Key Research and Development Program of China (No. 2017YFA0206301), and Beijing National Laboratory for Molecular Sciences (No. BNLMS202004).

Electronic Supplementary Material: Supplementary material (further details of OM imaging, AFM imaging, XRD measurements, TEM and SAED imaging, Raman spectra, energy band diagram, and DFT calculation) is available in the online version of this article at https://doi.org/10.1007/s12274-022-4543-8.

References

[1] del Alamo, J. A. Nanometre-scale electronics with III-V compound semiconductors. *Nature* **2011**, *479*, 317–323.

[2] Riel, H.; Wernersson, L. E.; Hong, M.; del Alamo, J. A. III-V compound semiconductor transistors—From planar to nanowire structures. *MRS Bull.* **2014**, *39*, 668–677.

[3] Li, D. P.; Lan, C. Y.; Manikandan, A.; Yip, S.; Zhou, Z. Y.; Liang, X. G.; Shu, L.; Chueh, Y. L.; Han, N.; Ho, J. C. Ultra-fast photodetectors based on high-mobility indium gallium antimonide nanowires. *Nat. Commun.* **2019**, *10*, 1664.

[4] Wang, X. Z.; Pan, D.; Sun, M.; Lyu, F. J.; Zhao, J. H.; Chen, Q. High-performance room-temperature UV–IR photodetector based on the InAs nanosheet and its wavelength- and intensity-dependent negative photoconductivity. *ACS Appl. Mater. Interfaces* **2021**, *13*, 26187–26195.

[5] Zhang, Y. Y.; Wu, J.; Aagesen, M.; Liu, H. Y. III-V nanowires and nanowire optoelectronic devices. J. Phys. *D Appl. Phys.* **2015**, *48*, 463001.

[6] Otnes, G.; Borgström, M. T. Towards high efficiency nanowire solar cells. *Nano Today* **2017**, *12*, 31–45.

[7] Li, Z. Y.; Tan, H. H.; Jagadish, C.; Fu, L. III-V semiconductor single nanowire solar cells: A review. *Adv. Mater. Technol.* **2018**, *3*, 1800005.

[8] Ko, H.; Takei, K.; Kapadia, R.; Chuang, S.; Fang, H.; Leu, P. W.; Ganapathi, K.; Plis, E.; Kim, H. S.; Chen, S. Y. et al. Ultrathin compound semiconductor on insulator layers for high-performance nanoscale transistors. *Nature* **2010**, *468*, 286–289.

[9] Al Balushi, Z. Y.; Wang, K.; Ghosh, R. K.; Vilá, R. A.; Eichfeld, S. M.; Caldwell, J. D.; Qin, X. Y.; Lin, Y. C.; DeSario, P. A.; Stone, G. et al. Two-dimensional gallium nitride realized via graphene encapsulation. *Nat. Mater.* **2016**, *15*, 1166–1171.

[10] Chen, Y. X.; Liu, K. L.; Liu, J. X.; Lv, T. R.; Wei, B.; Zhang, T.; Zeng, M. Q.; Wang, Z. C.; Fu, L. Growth of 2D GaN single crystals on liquid metals. *J. Am. Chem. Soc.* **2018**, *140*, 16392–16395.

[11] Ben, J. W.; Liu, X. K.; Wang, C.; Zhang, Y. P.; Shi, Z. M.; Jia, Y. P.; Zhang, S. L.; Zhang, H.; Yu, W. J.; Li, D. B. et al. 2D III-nitride materials: Properties, growth, and applications. *Adv. Mater.* **2021**, *33*, 2006761.

[12] Liu, Y.; Guo, J.; Zhu, E. B.; Wang, P. Q.; Gambin, V.; Huang, Y.; Duan, X. F. Maximizing the current output in self-aligned graphene-InAs-metal vertical transistors. *ACS Nano* **2019**, *13*, 847–854.

[13] Kim, T. W.; Kim, D. H.; del Alamo, J. A. Logic characteristics of 40 nm thin-channel InAs HEMTs. In *Proceedings of the 2010 22nd International Conference on Indium Phosphide and Related Materials* (*IPRM*), Takamatsu, Japan, 2010, pp 1–4.

[14] Sarkar, D.; Tao, J.; Ahsan, R.; Yang, D. Z.; Orvis, T.; Weng, S. Z.; Greer, F.; Ravichandran, J.; Sideris, C.; Kapadia, R. Monolithic high-mobility InAs on oxide grown at low temperature. *ACS Appl. Electron. Mater.* **2020**, *2*, 1997–2002.

[15] Hjort, M.; Lehmann, S.; Knutsson, J.; Zakharov, A. A.; Du, Y. A.; Sakong, S.; Timm, R.; Nylund, G.; Lundgren, E.; Kratzer, P. et al. Electronic and structural differences between wurtzite and zinc blende InAs nanowire surfaces: Experiment and theory. *ACS Nano* **2014**, *8*, 12346–12355.
[16] Liu, Z.; Luo, T.; Liang, B.; Chen, G.; Yu, G.; Xie, X. M.; Chen, D.; Shen, G. Z. High-detectivity InAs nanowire photodetectors with spectral response from ultraviolet to near-infrared. *Nano Res.* **2013**, *6*, 775–783.
[17] Shen, L. F.; Yip, S.; Lan, C. Y.; Shu, L.; Li, D. P.; Zhou, Z. Y.; Wong, C. Y.; Pun, E. Y. B.; Ho, J. C. Enhanced negative photoconductivity in InAs nanowire phototransistors surface-modified with molecular monolayers. *Adv. Mater. Interfaces* **2018**, *5*, 1701104.
[18] Ram, M. S.; Persson, K. M.; Irish, A.; Jönsson, A.; Timm, R.; Wernersson, L. E. High-density logic-in-memory devices using vertical indium arsenide nanowires on silicon. *Nat. Electron.* **2021**, *4*, 914–920.
[19] Takei, K.; Fang, H.; Kumar, S. B.; Kapadia, R.; Gao, Q.; Madsen, M.; Kim, H. S.; Liu, C. H.; Chueh, Y. L.; Plis, E. et al. Quantum confinement effects in nanoscale-thickness InAs membranes. *Nano Lett.* **2011**, *11*, 5008–5012.
[20] Grim, J. Q.; Bracker, A. S.; Zalalutdinov, M.; Carter, S. G.; Kozen, A. C.; Kim, M.; Kim, C. S.; Mlack, J. T.; Yakes, M.; Lee, B. et al. Scalable in operando strain tuning in nanophotonic waveguides enabling three-quantum-dot superradiance. *Nat. Mater.* **2019**, *18*, 963–969.
[21] Lu, H. Y.; Tian, S. C.; Tong, C. Z.; Wang, L. J.; Rong, J. M.; Liu, C. Y.; Wang, H.; Shu, S. L.; Wang, L. J. Extracting more light for vertical emission: High power continuous wave operation of 1.3-μm quantum-dot photonic-crystal surface-emitting laser based on a flat band. *Light:Sci. Appl.* **2019**, *8*, 108.
[22] Xu, T. F.; Wang, H. L.; Chen, X. Y.; Luo, M.; Zhang, L. L.; Wang, Y. M.; Chen, F. S.; Shan, C. X.; Yu, C. H. Recent progress on infrared photodetectors based on InAs and InAsSb nanowires. *Nanotechnology* **2020**, *31*, 294004.
[23] Larsson, M. W.; Wagner, J. B.; Wallin, M.; Håkansson, P.; Fröberg, L. E.; Samuelson, L.; Wallenberg, L. R. Strain mapping in free-standing heterostructured wurtzite InAs/InP nanowires. *Nanotechnology* **2007**, *18*, 015504.
[24] Cheng, R. Q.; Wen, Y.; Yin, L.; Wang, F. M.; Wang, F.; Liu, K. L.; Shifa, T. A.; Li, J.; Jiang, C.; Wang, Z. X. et al. Ultrathin single-crystalline CdTe nanosheets realized via van der Waals epitaxy. *Adv. Mater.* **2017**, *29*, 1703122.
[25] Wang, Q. S.; Safdar, M.; Xu, K.; Mirza, M.; Wang, Z. X.; He, J. Van der Waals epitaxy and photoresponse of hexagonal tellurium nanoplates on flexible mica sheets. *ACS Nano* **2014**, *8*, 7497–7505.
[26] Hang, Q. L.; Wang, F. D.; Carpenter, P. D.; Zemlyanov, D.; Zakharov, D.; Stach, E. A.; Buhro, W. E.; Janes, D. B. Role of molecular surface passivation in electrical transport properties of InAs nanowires. *Nano Lett.* **2008**, *8*, 49–55.
[27] Wang, F.; Wang, Z. X.; Shifa, T. A.; Wen, Y.; Wang, F. M.; Zhan, X. Y.; Wang, Q. S.; Xu, K.; Huang, Y.; Yin, L. et al. Two-dimensional non-layered materials: Synthesis, properties and applications. *Adv. Funct. Mater.* **2017**, *27*, 1603254.
[28] Zhao, B.; Dang, W. Q.; Liu, Y.; Li, B.; Li, J.; Luo, J.; Zhang, Z. W.; Wu, R. X.; Ma, H. F.; Sun, G. Z. et al. Synthetic control of two-dimensional $NiTe_2$ single crystals with highly uniform thickness distributions. *J. Am. Chem. Soc.* **2018**, *140*, 14217–14223.
[29] Zhao, X. X.; Yin, Q.; Huang, H.; Yu, Q.; Liu, B.; Yang, J.; Dong, Z.; Shen, Z. J.; Zhu, B. P.; Liao, L. et al. Van der Waals epitaxy of ultrathin crystalline PbTe nanosheets with high near-infrared photoelectric response. *Nano Res.* **2021**, *14*, 1955–1960.
[30] Li, N. N.; Zhu, L. L.; Shang, H. H.; Wang, F.; Zhang, Y.; Yao, Y. Y.; Wang, J. J.; Zhan, X. Y.; Wang, F. M.; He, J. et al. Controlled synthesis and Raman study of a 2D antiferromagnetic p-type semiconductor: α-MnSe. *Nanoscale* **2021**, *13*, 6953–6964.
[31] Sahoo, P.; Tyagi, A. K.; Raj, B.; Dhara, S. Surface optical modes in semiconductor nanowires. In *Nanowires—Implementations and Applications*; Hashim, A. A., Ed.; IntechOpen: London, 2011.
[32] Sunny, A.; Balasubramanian, K. Raman spectral probe on size-dependent surface optical phonon modes and magnon properties of NiO nanoparticles. *J. Phys. Chem. C* **2020**, *124*, 12636–12644.
[33] Prasad, N.; Karthikeyan, B. A Raman spectral probe on polar w-ZnS nanostructures and surface optical phonon modes in nanowires. *Nanoscale* **2019**, *11*, 4948–4958.
[34] Chen, S. S.; Liu, H. T.; Chen, F. H.; Zhou, K.; Xue, Y. Z. Synthesis, transfer, and properties of layered $FeTe_2$ nanocrystals. *ACS Nano* **2020**, *14*, 11473–11481.
[35] Habanyama, A. Interface control processes for Ni/Ge and Pd/Ge Schottky and Ohmic contact fabrication: Part one. In *Advanced Material and Device Applications with Germanium*; Lee, S., Ed.; IntechOpen: London, 2018.
[36] Kresse, G.; Furthmüller, J. Efficiency of *ab-initio* total energy calculations for metals and semiconductors using a plane-wave basis set. *Comput. Mater. Sci.* **1996**, *6*, 15–50.
[37] Kresse, G.; Furthmüller, J. Efficient iterative schemes for *ab initio* total-energy calculations using a plane-wave basis set. *Phys. Rev. B* **1996**, *54*, 11169–11186.
[38] Blöchl, P. E. Projector augmented-wave method. *Phys. Rev. B* **1994**, *50*, 17953–17979.
[39] Monkhorst, H. J.; Pack, J. D. Special points for Brillouin-zone integrations. *Phys. Rev. B* **1976**, *13*, 5188–5192.
[40] Kokalj, A. XCrysDen—A new program for displaying crystalline structures and electron densities. *J. Mol. Graphics Modell.* **1999**, *17*, 176–179.